Final Report

Project Title: **"Tunable Narrow Band Gap Absorbers For Ultra High Efficiency Solar Cells"**

Covering Period: May 2008 – April 2012

Date of Report: July 2012

Award Number: DE-FG36-08GO18072

Working Partners: Spectrolab Inc

Cost-Sharing Partners: North Carolina State University

Contacts: S. M. Bedair

Phone: (919) 515-5204

Email: bedair@ncsu.edu

Authors (NCSU): S. M. Bedair, P.I.; J. Hauser, N. Elmasry , Co-P.I.

P. Colter, Research Scientist

G. Bradshaw, C.Z. Carlin, J. Samberg, Grad Students

Author (Spectrolab): K. Edmonson, P.I.

DOE Project Team: Daniel Stricker

Executive summary

We report on a joint research program between NCSU and Spectrolab to develop an upright multijunction solar cell structure with a potential efficiency exceeding the current record of 41.6% reported by Spectrolab. The record efficiency Ge/GaAs/InGaP triple junction cell structure is handicapped by the fact that the current generated by the Ge cell is much higher than that of both the middle and top cells. We carried out a modification of the record cell structure that will keep the lattice matched condition and allow better matching of the current generated by each cell. We used the concept of strain balanced strained layer superlattices (SLS), inserted in the i-layer, to reduce the bandgap of the middle cell without violating the desirable lattice matched condition. For the middle GaAs cell, we have demonstrated an *n*-GaAs/*i*-(InGaAs/GaAsP)/*p*-GaAs structure, where the $In_xGa_{1-x}As/GaAs_{1-y}P_y$ SLS is grown lattice matched to GaAs and with reduced bandgap from 1.43 eV to 1.2 eV, depending upon the values of x and y.

We have utilized several unique approaches in this demonstration. In particular, a) the use of GaAsP with GaP% as high as 80% that will allow both high values of InAs% and thicker InGaAs wells b) carrier transport by tunneling that allows the absorbing InGaAs layers to constitute close to 70% of the i-layer. c) a staggered strained layer superlattice to minimize the quantum size effect.

We have found that the addition of an InGaAs/GaAsP SLS to a GaAs cell achieves an improvement in J_{SC} by 3.5 mA/cm^2 (≈4.5 mA/cm^2 corrected for AR coating) with only a 30 mV reduction in V_{OC}. Additionally, tandem cells with an InGaP top cell grown by Spectrolab on top of our GaAs+SLS cell show that the current generated by the GaAs+SLS cell is 2 mA/cm^2 in excess of the top cell. Also the EQE of the InGaP top grown on NCSU SLS structure is close to the standard top cell grown at Spectrolab. The significance of these results is that in a fully optimized three-junction cell every additional 1 mA/cm^2 in the middle cell will result in an increase of η of about 2%.

The report is organized in two parts. The first part deals with fundamental material issues of the growth of the SLS with both high InAs% and GaP%. This is followed by modeling and predictions about the SLS performances, the QSE, the effect of staggering and carrier transport via tunneling. This is followed by the device results. The second part, prepared by Spectrolab, present data about the two junction tandem cell with the GaAs cell augmented by the SLS to extend the absorption to about 1 micron.

I. Background and rationale

Recent progress on three junction cells using GaInP(1.9eV)/GaAs(1.43eV)/Ge(0.67eV) has led to conversion efficiency of 42% at high solar concentration [1-3]. In this structure the sub cells are nearly ideally efficient for their bandgaps but the solar spectrum between the GaAs and Ge band gaps is not effectively utilized; the Ge cell has about twice the current available as the other cells. Several approaches have been tried to improve the solar spectrum utilization.

It has been realized that high conversion efficiency with nearly ideal spectrum utilization can be achieved in three and four junction structures [4]. The four junction cell requires a materials systems with band gaps E_g: 1.9 eV/1.5 eV/1.0 eV/0.67 eV(Ge) while the three-junction requires a material with an effective bandgap of 1.2 eV for the middle cell. Material systems with E_g > 1.43 eV and lattice matched to GaAs (or Ge) are readily available such as (Al)InGaP, GaInAsP and AlGaInAs. However, a material system that collects photons in the 1.4 eV to 1.0 eV range and is lattice matched to GaAs (or Ge) has proven to be very difficult to achieve. Several approaches have been investigated to address the 1.0-1.4 eV sub cell problem. The first approach relies on the addition of N to GaAs to form GaAsN to reduce E_g to ~1.0 eV while maintaining the lattice matched conditions to GaAs [5,6]. A nitrogen content exceeding the solubility limit results in material with poor quality GaAsN that suffers from both poor diffusion length and minority carrier lifetime. MBE results have shown efficiency improvement and 43% has been reported. However, MBE is a more expensive approach and may have difficulty in meeting the $1/watt DOE goal. A second approach to improving the spectrum utilization uses metamorphic material that is slightly lattice mismatched to GaAs. Replacing GaAs by $In_xGa_{1-x}As$ (x~8%) extends the absorption range and collects photons down to 1.38 eV resulting in an improvement in the conversion efficiencies. It is expected that it will be difficult to push the value of x high enough to achieve full spectrum utilization while maintaining device quality material through a stack of several junctions (the GaInP top cell is particularly sensitive to defects). The third approach uses an inverted structure. The top GaInP is grown first on the GaAs substrate, then the lattice constant is graded to grow $In_{0.3}Ga_{0.7}As$ (E_g = 0.9 eV) followed by etching off the GaAs substrate [7]. Record efficiency of 43% had been reported. The main problem with this approach is the separation (substrate removal) and handling an ultra-thin film in large scale production.

I-1 Proposed approach

A fourth approach using an InGaAs/GaAsP strained layered superlattice, lattice matched to GaAs is the focus of this project. InGaAs strained films with thicknesses ~5-10 nm are the light absorbing layers and GaAsP form the strain balancing layers. This approach has been used successfully to partially absorb 9photons in the 1.4-1.2 eV range and improve the short circuit current (J_{SC}) [8,9]. In order to achieve the full potential of this approach we are pursuing an approach which uses ultra-thin barriers to allow tunneling transport of carriers. This unique approach, when optimized, will allow greater efficiency and thinner (and potentially cheaper) structures than alternative superlattice approaches.

The new sub cell structure is designed to collect photons in the energy range 1.4-1.1 eV while maintaining the lattice matched conditions. The projected practical efficiency is up to about 45%.

NCSU has worked to develop the new sub cell and Spectrolab has integrated prototype sub cells into their multi-junction structures.

I-2 Factors affecting material choices

The multilayer tunable absorber made of InGaAs/GaAsP has been designed to satisfy the following materials and device requirements to achieve high conversion efficiency. There are several factors that need to be addressed.

a) Critical layer thickness (CLT): The InGaAs films are strained to equal to the lattice constant of GaAs, or Ge which has a lattice constant equal to $Ga_{0.99}In_{0.01}As$. The thicknesses of these absorbing InGaAs layers need to be less than the critical layer thickness (CLT), the point at which misfit dislocations form in the film due to material relaxation, to maintain the high quality of the InGaAs films [10]. The CLT depends critically on the value of x. For example; for x = 3%, 10% and 30%, the approximate corresponding values of CLT are 100 nm, 18 nm, and 5 nm, respectively.

b) Strain balance: Due to CLT limitations, multilayers of $In_x Ga_{1-x}As$ are to be used to enhance photon absorption. For values of x larger than few percent, we introduce $GaAs_{1-y}P_y$ films under tensile strain to balance the compressive strain in the InGaAs layers. This results in a structure with an in plane lattice constant equal to that of GaAs or Ge [11]. The value of y and thicknesses of GaAsP films t_p will be selected to enhance the thickness of the InGaAs absorbing layers and allow carrier transport with internal quantum efficiency ~100%. High values of y allow thicker InGaAs absorbing films. The value of y in the $GaAs_{1-y}P_y$ layers will be in the range 60-80% with layer thickness t_p of 2-3 nm. The presence of a high band discontinuity (ΔE_g) between InGaAs and GaAsP layers will require very thin GaAsP barriers for efficient carrier transport by tunneling. The lattice mismatch of GaP to GaAs (tensile strain) is about one half of the lattice mismatch between InAs to GaAs (7% compressive strain). It can be shown that, to maintain the strain balanced with GaAsP, the thickness of InGaAs films (t_{In}) is given by $t_{in}(\text{Å}) = 50t_p/x$.

c) Carrier transport: Carrier transport through the very thin t<4nmhigh band gap GaAsP barriers, is not well studied. The effects of barrier thickness and composition (in the high phosphorus regime) on the tunneling transport of carriers must be modeled and verified experimentally in order to design an optimal structure realizing the potential advantages of a tunneling transport device.

d) Quantum size effects: For high values of x fairly thin InGaAs films are needed due to satisfy both the CLT and the strain balance requirements. Since the InGaAs layers are very thin (t < 7 nm) and surrounded by high band gap GaAsP barriers, QSE (quantum size effect) will increase the effective value of E_g of the well. This increase in E_g is not desirable if low energy photons are to be absorbed. However the QSE is reduced since thin GaAsP barriers (2-3 nm) allow the wave functions to overlap between wells and minibands will be formed rather than discrete energy levels.

I-3 Implementation

Taking into consideration the materials considerations for multilayer tunable absorbers made of InGaAs/GaAsP just discussed the following tasks have been performed:

Material Development

1) **Composition calibration:**
2) **Doping calibration**
3) **Strain balance (modeling and calibration)**
4) **Characterization by optical microscopy, X-ray diffraction and TEM**

Modeling

1) **Modeling of transport**
2) **Modeling of optical absorption**

Device fabrication and characterization

***1*) Cell Structure fabrication**

2) Spectral response characterization

3) Light I-V characterization

4)Experimental study of barrier thickness effects

II. Growth and material characterization

II-1 Compositional Calibration

To determine the composition of the various ternary alloys ($In_xGa_{1-x}As$, $GaAs_{1-x}P_x$ and $Al_xGa_{1-x}As$) a linear interpolation, Vegard's law, of Bragg's law ($n\lambda = 2d \sin\theta$) was utilized using the appropriate two binary compounds as endpoints for X-ray diffraction analysis. However, to effectively use this model one must know if the film is relaxed or strained. The relaxation of the film was determined via optical microscopy and will be discussed in more detail later. When films relax the physical manifestation of the relaxation produces characteristic cross hatching on the surface. For films that display such a characteristic cross hatch, 100% relaxation is assumed and a straight linear interpretation of Bragg's law can be assumed. However, for films where no physical relaxation is observed (no cross hatch), one must take into account the Poisson's ratio of the material as it relates to the XRD data. This results in a multiplication factor of $(1-\nu)/(1+\nu)$ for symmetric (004) reflections. Most materials have Poisson's ratios of $\nu=0.33$ resulting in multiplication factors of ½. This non-relaxation occurs between materials with very small mismatch such as $Al_xGa_{1-x}As$ on GaAs. For materials with larger mismatch, such as InGaAs or GaAsP on GaAs, the composition analysis is very straight forward as 100% relaxation is easy to achieve. It should be noted that temperature plays a very important part in determining the compositions of these ternary alloys, especially in the case of GaAsP. As temperature increases, the incorporation of the phosphorus (P from TBP) increases, and results in a ternary alloy with greater P composition. Consequently, as the temperature is decreased the incorporation of the(P fromTBP) decreases, which decreas the P/As ratio and results in a ternary alloy with greater As composition. This means it was necessary that calibration curves for both GaAsP and InGaAs be constructed each time a thermocouple was changed as shown in figures II-1 and II-2. Additionally there is a compromise in the temperatures at which the two constituents of the SLS are best grown.

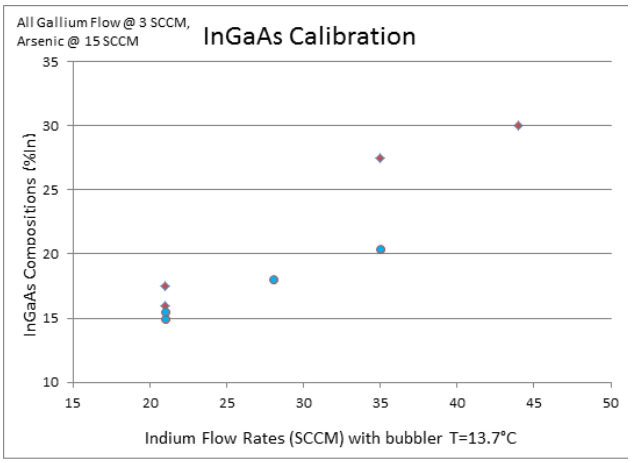

Figure II-1: In calibration curves showing recalibrations after thermocouple change

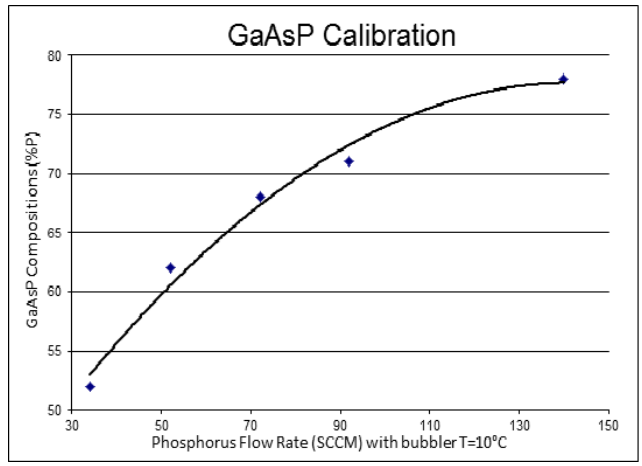

Figure II-2: Phosphorus calibration showing saturation of phosphorus content at 75-80%

II-2 Doping Calibration

Doping Calibrations for the following dopants in GaAs were undertaken: Si, Zn, and C. Hall measurements were performed to determine the doping levels for each dopant. The Hall Effect, for a conductor, is the production of a potential difference, V_H, transverse to a current in the presence of a magnetic field, B. This magnetic field must be perpendicular to the current to drive the carrier. The magnetic field causes the creation of an electric field, E_H, that balances the Lorentz force exerted on the carriers. This electric field is orthogonal to both the magnetic field and current and is directly related to the two which is then directly related to the Hall voltage, the voltage resulting from E_H. This gives the following equation:

$$V_H = \frac{R_H I B}{t}$$

which can be used to determine the carrier type, where V_H is the Hall voltage, R_H is the Hall resistance, I the current, B the magnetic field and t the film thickness. The carrier type is determined by the sign on both the V_H and R_H. Additionally the carrier concentration can be determined from:

$$R_H = \frac{r_p}{pq} \; or - \frac{r_n}{nq}$$

depending on the carrier type.

In order to allow measurements on easily prepared samples an apparatus which allowed switching of the current as described by van de pawl was used.Hall samples were grown on semi-insulating substrates. This allows for the properties of the film alone to be measured. Top contacts were made with indium dots. Gold wires were then used to connect the samples to the Hall setup. This setup made it possible to determine the type and concentration levels for each dopant. Doping calibrations were undertaken for each level of a device structure for both p/n and n/p polarities. The calibration curves for Si, Zn and C are presented in Figures II-3, II-4 and II-5 respectively. Data for Zn calibration are good enough for both the base and emitter for both n/p and p/n structures studies in this project

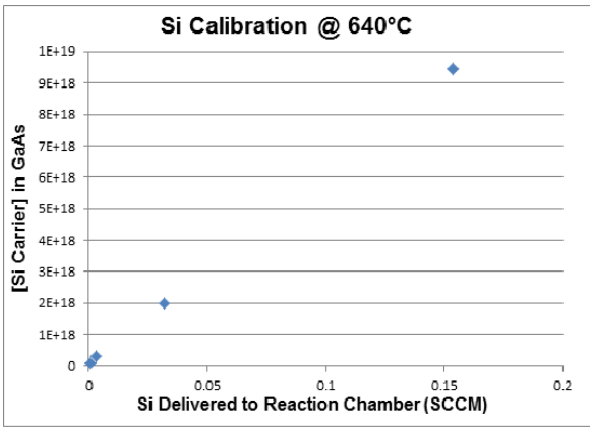

Figure II-3: Silicone Doping Calibration Curve for GaAs

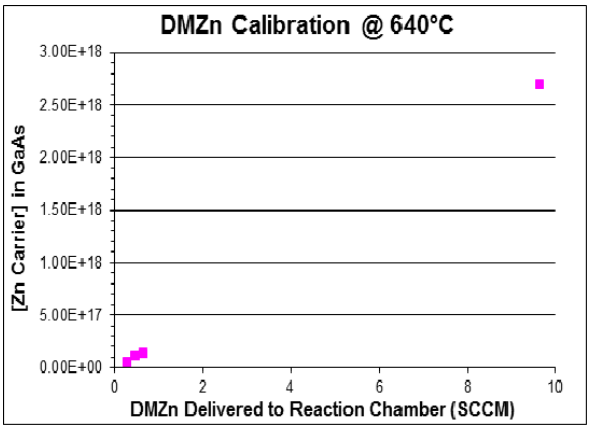

Figure II-4: Zinc Doping Calibration Curve for GaAs

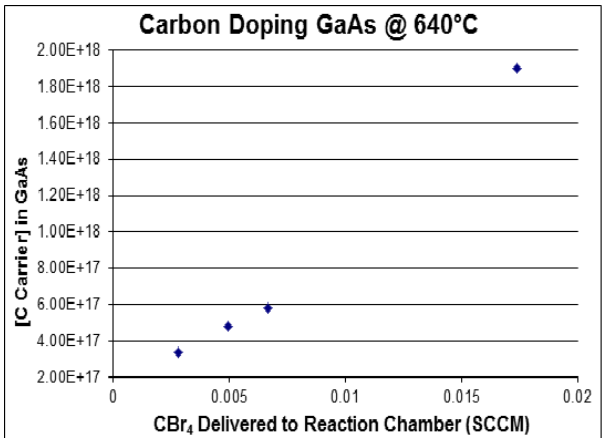

Figure II-5: Carbon Doping calibration for GaAs

II-3 Strain/Stress Balance

For growth of strain balanced strain-layer structures (SLS) there are three main balancing models. The first of these models is the average lattice method. This model arises from the notion that the strain-balance structure can be assumed to be the thickness average of the compressive and tensile lattice parameters and is derived directly from Matthews and Blakeslee's original paper [10]. It also assumes the elastic properties of the layers are identical. However, this assumption is also the main drawback of this approach and is really only valid for a limited set of SLS tensile and compressive materials. The second method is the thickness weighted method and while it does take into account the different elastic constants for various materials, it does not provide the most accurate of balancing. In the end, the main goal of a strain-balance model should be to achieve a zero average in-plane stress condition in the tensile/compressively strained layer combination. This is most accurately done, assuming abrupt interfaces, by using the zero-stress balance method. From classical elastic theory the zero-stress balance equation is derived as: [12]

$$a_0 = \frac{A_1 t_1 a_1 a_2^2 + A_2 t_2 a_2 a_1^2}{A_1 t_1 a_2^2 + A_2 t_2 a_1^2}$$

where a_0, a_1 and a_2 are the lattice constants for the substrate, compressive and tensile material respectively. Additionally, t_1 and t_2 are the thicknesses of the compressive and tensile strained layers and A_1 and A_2 are constants for each layer determined by their respective elastic stiffness coefficients:

$$A = C_{11} + C_{12} - \frac{2C_{12}^2}{C_{11}}$$

When dealing with ternary compounds it is assumed that the elastic coefficients, C_{11} and C_{12}, can be linearly interpolated from the two binary materials comprising the ternary compound. However, while this is fairly accurate near the peripheries (~20%) of the ternary compound composition, it becomes problematic the farther one shifts from the peripheries as many ternary compounds have unknown bowing parameters that should be considered. Additionally, the zero-stress balance equation is based solely on a strain energy analysis and does not take into consideration any kinetic barriers that may occur during growth. Data for the dependence of well width and barrier thickness for different InAs% in the well and 80% GaP in the barrier are shown in Fig II-6

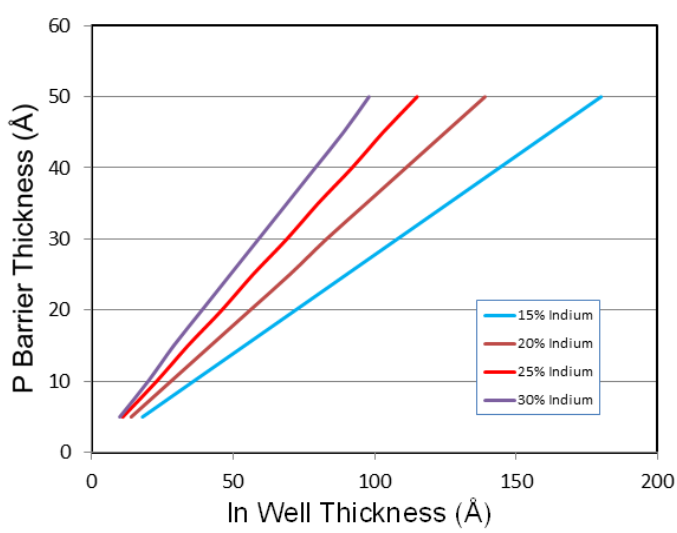

Figure II-6: Well and barrier thicknesses for balanced superlattices with 80% phosphorus and various indium concentrations.

However, using the zero-stress balance method, very thin SLS (92Å/30Å of $In_{17.5}Ga_{82.5}As/GaAs_{20}P_{80}$ respectively) have been successfully grown and balanced. The best ways to determine if stress-balance pseudomorphic growth has been accomplished is by investigation via optical microscopy and x-ray diffraction, both of which will be discussed later.

II-4 Optical Microscopy

Perhaps the most important characterization technique for the SLS under investigation is that of optical microscopy. While qualitative in nature, optical microscopy can yield a great deal of information about a sample. High quality films of this materials system appear specular and smooth at high magnifications and have a mirror like finish at lower magnifications. Ex-situ cleaning issue can easily be diagnosed as can growth issues resulting in hazy, pitted, or rough surfaces. Additionally, misfit dislocations can be observed using optical microscopy. In zinc-blend systems the misfit dislocations are inclined at 60° along two <110> directions orthogonal to one another. It is well documented that strain is relieved along these directions. The physical manifestations of this strain relaxation can easily be viewed via optical microscopy. The absence of such misfit dislocations indicates that good pseudomorphic growth was achieved. Additionally, if misfit dislocations are observed, it is possible to determine the type of strain which resulted in the relaxation. There are two main types of strain, tensile and compressive. Each of these strains results in a characteristic relaxation. When a tensile zinc blend film relaxes it produces discontinuous lines in one direction and continuous lines in the other, figure II-7a. When a compressive zinc blend film relaxes the physical manifestation is that of continuous lines in both <110> directions, figure II-7c. Figure II-7b is the picture of a stress-balanced SLS and has thus not relaxed.

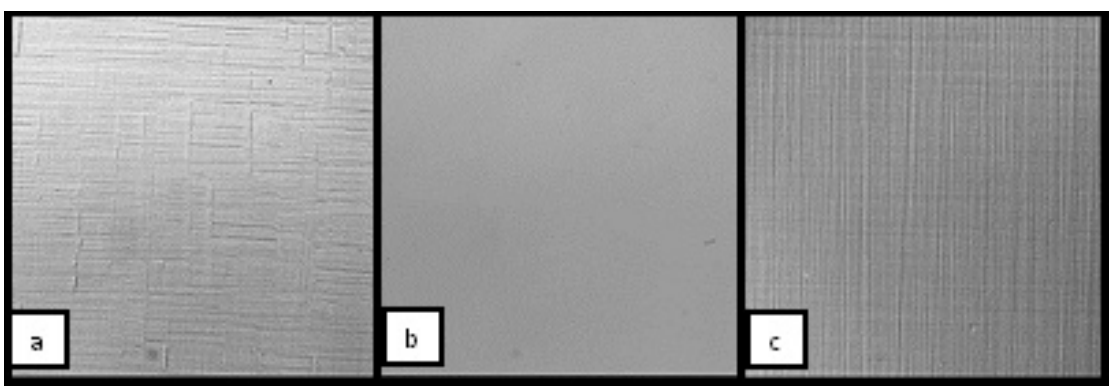

Figure II-7: The pictures of tensile relaxation (a), compressive relaxation (c) and a SLS that is pseudomophically grown (b)

II-5 SLS XRD analysis

X-ray diffraction (XRD) is one of the primary tools for materials characterization of the SLS. The x-rays interact with the crystal structure of the SLS to form satellite fringes with increasing FWHM moving away from and centered around the 0th order peak, figure I-8. These satellite fringes are periodic and can be used to determine the thickness of a period in the SLS by:

$$\sin(\theta_{n\pm1}) - \sin(\theta_n) = n\lambda/(2\mathrm{t})$$

Where sin ($\theta_{n\pm1 \text{ or } n}$) is the Bragg angle for the n+1 or n satellite fringe, λ is the source wavelength and t is the thickness of each period and is comprised of the In wells, P barriers and GaAs transition layers. Thus it is possible to determine the thickness of the individual layers in the SLS if one knows the composition of the individual layers as well as the growth times. This is because the III species are limiting reagents in the growth rate of the structure. So while the GaAsP growth rate is the same as it is for GaAs, the InGaAs growth rate is related directly to the composition of the In. So an Indium composition of $In_{.5}Ga_{.5}As$ will give a growth rate twice that of GaAs assuming the same TMG flow rate is used.

Some of the superlattices had what is called a 'staggered' structure, which will be discussed further in sections III and IV, but for the purpose of materials analysis, had a period twice that of a regular superlattice. This results in the satellite fringes being spaced much closer together (density increases by a factor of 2) than is seen in the XRD of a normal SLS. Figure II-8 shows the 2θ-ω for normal and staggered superlattices.

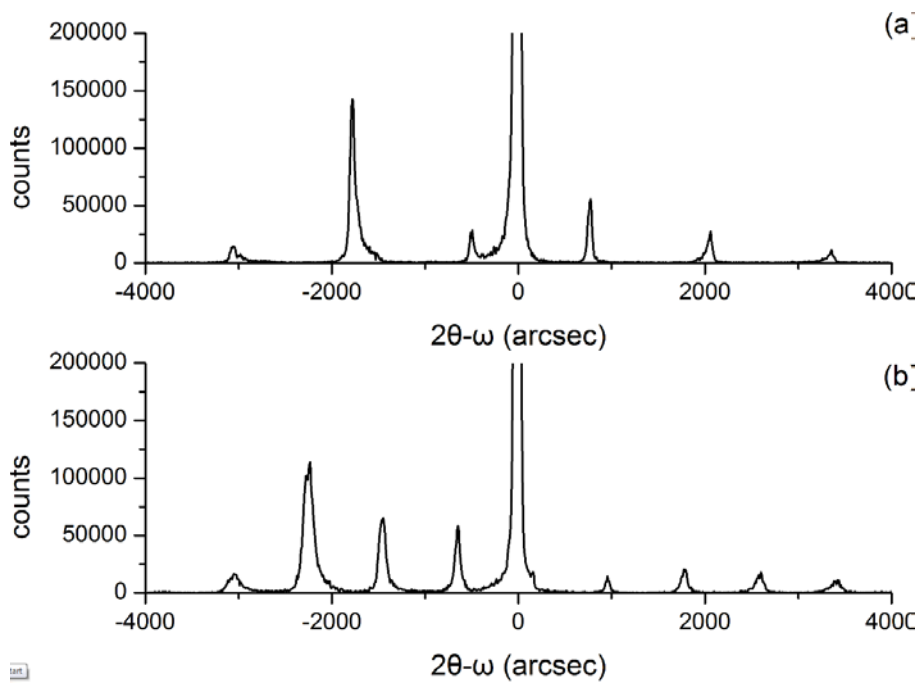

Figure II-8: 2θ-ω XRD scans of (a) a standard, strain balanced SLS and (b) a strain balanced staggered SLS

II-6 TEM Analysis

Due to the time consuming nature of transmission electron microscopy (TEM) sample preparation, TEM was not used as a primary characterization method, but rather as a secondary characterization method to support the other methods of characterization. TEM was used to determine the control with which each period can be grown in the SLS as seen in figure II-9a. While the results from this TEM image do not match exactly with that obtained from the XRD data, it is well within reason. The most probable reason

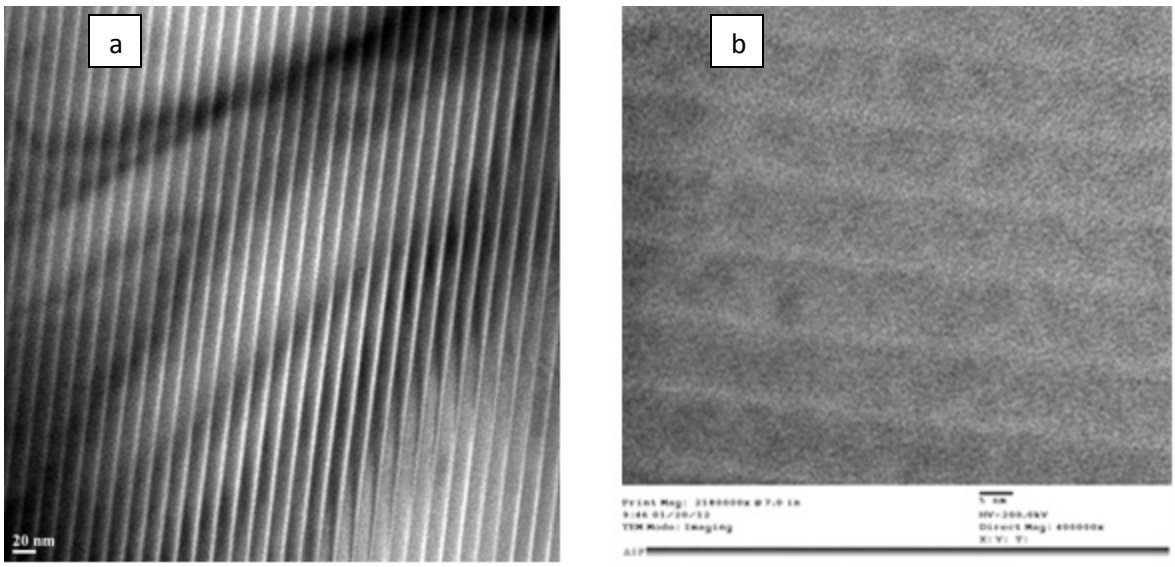

Figure II-9: Bright field TEM cross-sectional image of a SLS (a) and HRTEM image of SLS interfaces (b). In each case the P barriers are represented by the lighter regions with the In wells being darker

for the discrepancy is a slight miscalibration of the TEM itself. High resolution TEM (HRTEM) was used to investigate the interfaces of the SLS, with respect to point defects, as demonstrated in figure II-9b. In this image the atoms are represented by the brighter areas and no interfacial defects are observed at this magnification. Another characterization method that is closely related to TEM is scanning TEM (STEM). STEM has many advantages over TEM that include: directly interpretable images, high Z contrast, larger area investigated due to rastering the electron beam. Using STEM it is possible to look at the diffusivity of the interfaces in much more detail than can be obtained from TEM. Initial STEM analysis indicates the interfaces are not as crisp as would be expected for perfect interfaces lacking diffusion. However, it is unclear if this diffusivity is due to diffusion or if it is an artifact created by the GaAs transition regions in the SLS. Another possible reason is the gas switching between two column V compounds which is known to compromise interface sharpness. The Z contrast between 15% InGaAs and GaAs is not very high. More research into improving the interface diffusivity of the SLS should be undertaken.

II-7 Future Work

While a lot of work has been accomplished, more still needs to be done. For the best possible extension, it is necessary to use high content InGaAs. Doing this greatly complicates the zero-stress balance due to unknown bowing parameters for the elastic coefficients of the ternary alloys. Additionally, while bulk calibrations are easy to characterize, it is still unclear if the compositions within the SLS for both the wells and barriers are that which are obtained for bulk growth. There is strong evidence indicating that the wells are much lower in In content than is expected. However, if this is the case, it must also be true that the barriers are lower in P content in order for the structure to follow the zero-stress balance model. Electron beam induced current should be utilized to determine the diffusion lengths of the carriers for both P/N and N/P device polarities. Interface abruptness needs to be investigated in two

main regards. First, the formation of abrupt interfaces must be studied and obtained. Next, the abruptness of the interface must be studied with respect to device characteristics.

III. Modeling

Modeling was used in this project to optimize the superlattice structure and to explain the optical and electrical behavior of fabricated devices. The work focused on maximizing the absorption of the superlattice while ensuring that it did not degrade the electrical performance of the p-i-n diode structures. Figure III-1 shows the band structure of a superlattice device. The superlattice itself is composed of alternating layers of GaAsP, which provide tensile strain and act as barriers to carrier transport and InGaAs, which add compressive strain and absorb light below the band gap of GaAs to produce electrons and holes. As previously mentioned, the composition and thickness of these two layers must be tuned so that the strain in the InGaAs balances the strain in the GaAsP and that neither layer exceeds its critical layer thickness. The requirement of strain balance adds a constraint which limits the superlattice structures that can be considered to balanced superlattices, since any unbalanced structure will produce a large number of defects which will degrade the electrical performance of a device. There are three other factors which must be considered in superlattice design. First, since the GaAsP is used with high phosphorus content, transport occurs by the tunneling of carriers through the barrier rather than thermionic emission over the barrier. This means that there is a minimum thickness to the GaAsP barrier and, due to strain balancing, the InGaAs wells. The second factor arises due to the limitation on the well thickness. As a quantum well is made thinner, the energy of the confined states increases, effectively increasing the band gap, a phenomenon known as the quantum size effect (QSE). Since the goal of this project is to reduce the band gap in the GaAs subcell, the QSE is undesirable. Lastly, the superlattice must be placed in a region with a high electric field, i.e. the intrinsic region of a p-i-n structure. The thickness of this high field region is limited by unintentional doping in the superlattice which limits its thickness to about 1 µm. The goal of modeling was to work within these constraints to design a structure which maximizes the current output of the SLS-GaAs cell.

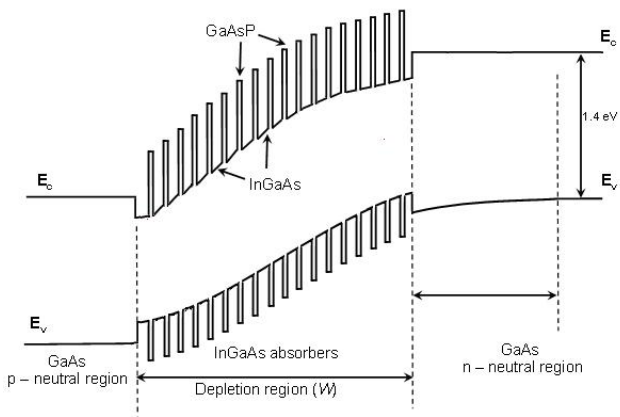

Figure III-1: InGaAs/GaAsP strained layer superlattice in the intrinsic region of a p-i-n device

III-1 Barrier thickness and carrier transfer mechanism

One of the previously mentioned constraints on the superlattice design is the thickness of the barriers since transport through the superlattice is believed to occur by tunneling. However, in order to maximize the well thickness, it was necessary to confirm this assumption and to determine how thick the barriers can be grown before the increase in tunneling lifetime began to degrade the performance of the device. The average time it takes a carrier to escape a well by tunneling is: [13]

$$\frac{1}{\tau_{tn}} = \frac{n\hbar\pi}{2L_w^2 m_w^*} e^{-\int_0^{L_b} \sqrt{2m_b^*(E_b - Fz)}dz/\hbar}$$

where L_b, the barrier width, is the most important factor with E_b (barrier height) and m^*_b (barrier effective mass) being of secondary importance. For thermionic emission the relation is: [14]

$$\frac{1}{\tau_{th}} = \sqrt{\frac{kT}{2\pi m_w^* L_w^2}} e^{-E_b/kT}$$

which has a stronger dependence on barrier height than the tunneling lifetime. For efficient transport, the carrier must escape the well before it can recombine. The escape probability, or internal quantum efficiency (IQE) can be found with

$$IQE_1 = \tau_E^{-1}/(\tau_E^{-1} + \tau_R^{-1})$$

where τ_E is the escape lifetime (either tunneling or thermionic emission) and τ_R is the recombination lifetime, which was taken to be 100 ns. In order to achieve a high IQE, the tunneling lifetime should be much shorter than the recombination lifetime. For a superlattice of N wells the total IQE is the IQE of one well to the Nth power. Using these equations the IQE can be found for a given superlattice both by tunneling and thermionic emission [15]. A superlattice is useful only if it shows no degradation in performance relative to a simple GaAs device, which means the IQE should be close to 1. Table III-1

Table III-1: Tunneling escape probability for electron and heavy hole states for a single well and for a 20 well device

Barrier thickness	Number of wells	Tunneling escape probability			
		e1	e2	hh1	hh2
25Å	1	0.9998	0.99998	0.9998	0.9999
	20	0.997	0.9996	0.996	0.998
41Å	1	0.971	0.993	0.991	0.996
	20	0.552	0.873	0.832	0.930

Table III-2: Thermionic emission escape probability

Temperature (K)	Barrier Thickness	e1	e2	hh1	hh2
290	25Å	0	0.773	0.597	0.791
	41Å	0	0	0.419	0.618
373	25Å	0.035	0.973	0.942	0.968
	41Å	0	0.165	0.903	0.938

Table III-3: Tunneling and thermionic emission escape probability for electrons at various reverse bias potentials

Bias (V)	Energy levels (meV)		Tunneling probability		Thermionic probability	
	e1	e2	e1	e2	e1	e2
0	44.8	106	0.552	0.873	0	0
-1.5	67.0	134	0.659	0.919	0	0
-3	86.9	162	0.744	0.950	0	0.008

shows the probability of escape by tunneling while table III-2 is the escape probability by thermionic emission. Results are given for the first two electron states and the first two heavy hole states. It can be seen from the two tables that tunneling results in a higher IQE than thermionic emission for devices with both thin and thick barriers. It is expected then that the barrier thickness will be an important consideration in superlattice design. The tunneling IQE has also been calculated at several values of

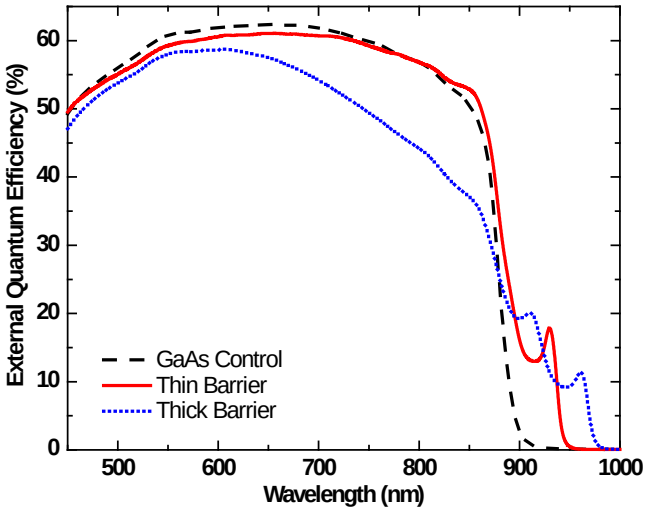

Figure III-2: EQE of standard device and SLS devices with different barrier thicknesses

reverse bias, as given in table III-3, which shows an enhancement in tunneling lifetime with increasing electric field.

To test this with actual device parameters two lattice-matched devices on p-type substrates with 27 Å ('thin') and 41 Å ('thick') barrier thickness SLSs of 20 periods were grown, fabricated and tested to find the IV and EQE response. Additionally, the IQE by tunneling and thermionic emission from the first and second hole states and first and second electron states were calculated. This can be seen in the EQE of the two devices seen in figure III-2 where thick barrier device shows a decrease in the EQE relative to the GaAs standard and the thin barrier device. It should be noted that the decrease in EQE is stronger at long wavelengths. Due to low absorption in GaAs in this region of the spectrum, the poor transport must be due to the minority carriers generated in the base, which are electrons. This is consistent with the results in table I which show a lower IQE for electrons than holes. The EQE was also found for both devices in reverse bias, as figures III-3 and III-4 show. The EQE is unchanged for the thin barrier device since the IQE is already unity at 0 V. However, the thick barrier device shows the enhancement predicted in table III-3. Figures III-5 and III-6 show the EQE of the two devices at raised temperatures. The thin barrier device, as in the reverse bias experiment, shows no EQE enhancement at higher temperature while the thick barrier device does. This is consistent with the higher IQE calculated in table III-1 for the second electron state since this state is more highly occupied at elevated temperature. These results suggest that transport proceeds through a field- and thermally-assisted tunneling

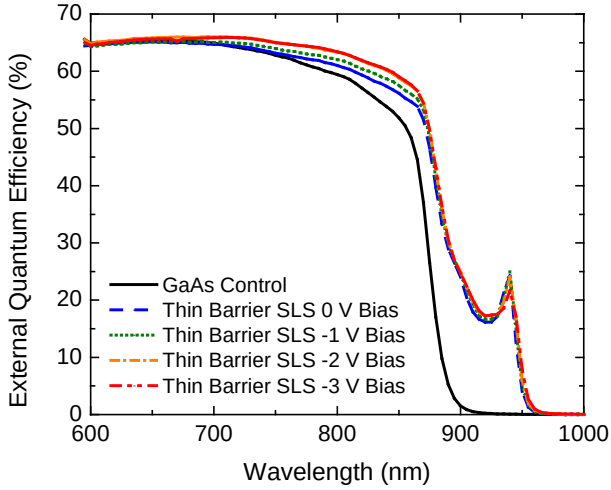

Figure III-3: EQE at several reverse biases for thin barrier SLS device

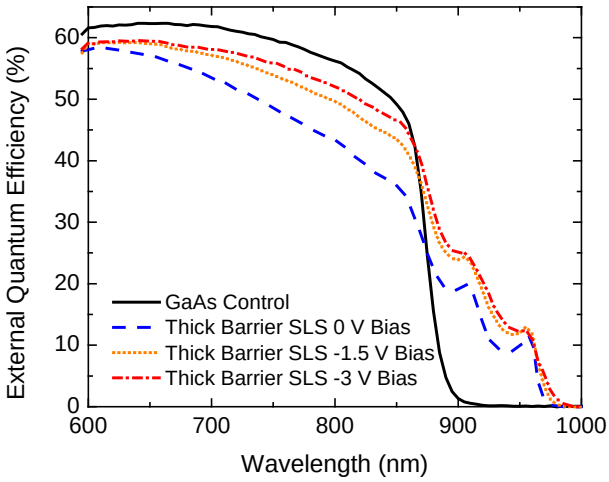

Figure III-4: EQE at several reverse bias voltages for thick barrier SLS device

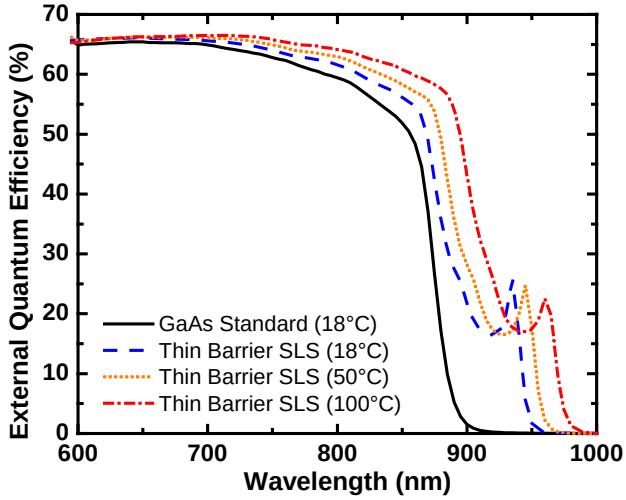

Figure III-4: EQE of thin barrier device at elevated temperature

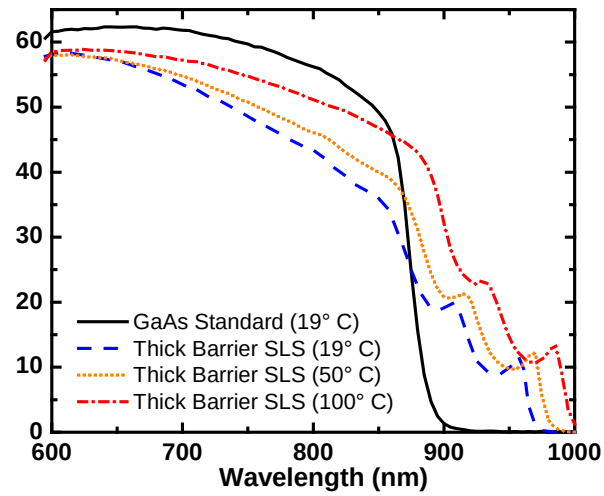

Figure III-5: EQE of thick barrier device at elevated temperature

mechanism. The barrier thickness is limited to about 30 Å, a value which is supported both by modeling and experimental evidence. Given the field and temperature tunneling mechanism, a graded barrier which is thinner at the top than the bottom would be advantageous. The GaAs intermediate layers used in our superlattices are believed to give such a structure.

III-2 Band edge modeling

Once the barrier thickness is set, it is useful to determine the expected extension in the EQE from the superlattice. There are several factors which change the band edge relative to absorption in bulk InGaAs. The most important factor, and the one that was most extensively investigated, is the quantum size effect. The QSE can be taken into account simply by using the finite quantum well model, but this does accurately account for the effect of electric field and non-abrupt interfaces. These factors can be dealt with by solving the Kronig-Penny model, which is used to find the dispersion relationship for flat, abrupt interface superlattices, but can be adapted to a general model which can be applied to superlattices of any shape. From the dispersion relationship the energy of all bound states can be found for a particular carrier. In addition, the decrease in the heavy hole energy due to compressive strain in the well must be considered.

The generalized Kronig-Penny model gives a solution to the envelope function approximation of the superlattice wave function which satisfies boundary conditions which maintain the continuity of the wave function and its derivative. These solutions can be written as a transfer matrix with the form [16]

$$\Gamma = \begin{bmatrix} \cos(kz) & \frac{m^*}{k}\sin(kz) \\ -\frac{k}{m^*}\sin(kz) & \cos(kz) \end{bmatrix}$$

Where m* is the effective mass of the material and $k = \sqrt{2m^*(E-V)/\hbar^2}$. Since E-V is positive in the well the transfer matrix elements have a sinusoidal form, since it is negative in the barrier the elements are exponentials. The product of the transfer matrices for an N-layer superlattice is found ($\Gamma = \Gamma_1\Gamma_2\cdots\Gamma_N$) and the dispersion equation for the superlattice is given by ½Tr(Γ). The individual states are given by the zero crossings of this equation. This equation can be used to find both electron and light or heavy hole states.

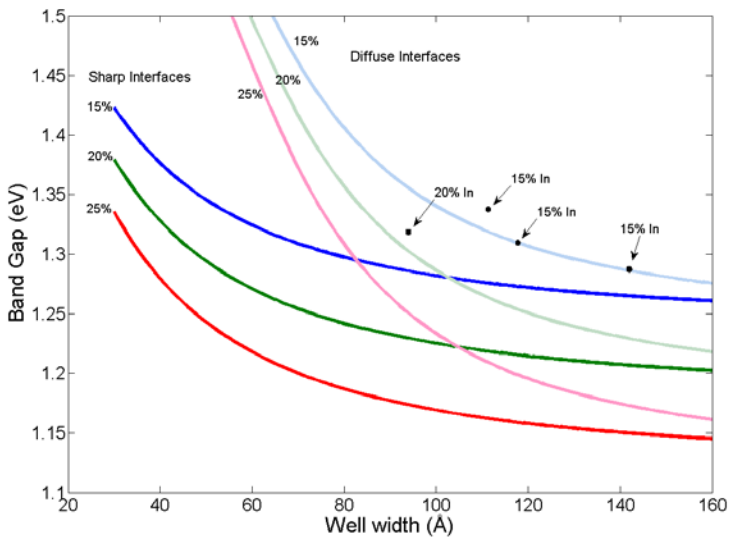

Figure III-6: Predicted band edge with and without graded interfaces. Experimental values shown to agree with graded SLS model.

Initial calculations which modeled the superlattice as a flat structure with abrupt interfaces between the barrier and well resulted in a predicted band edge which was at a lower energy that what was found in actual devices. It had been previously found that the addition of a ~7Å GaAs layer at each superlattice interface improved the material and electrical properties of SLS devices. This, along with indium segregation and gas switching, produce a graded interface which was taken into account when modeling the superlattice band gap. While a constant energy region results in an exponential or sinusoidal wave function, as shown above, graded region give solutions in terms of Airy functions. The transfer matrix for the graded layers is too complicated to give here, but it results in a similar dispersion relationship as the constant energy formulation. The two forms of the transfer matrix can be combined for superlattices which contain both flat and graded regions. It has been found that a grading of 20 Å in a 30 Å barrier device results in a good agreement with the quantum well energy found from experiment, as seen in figure II-6.

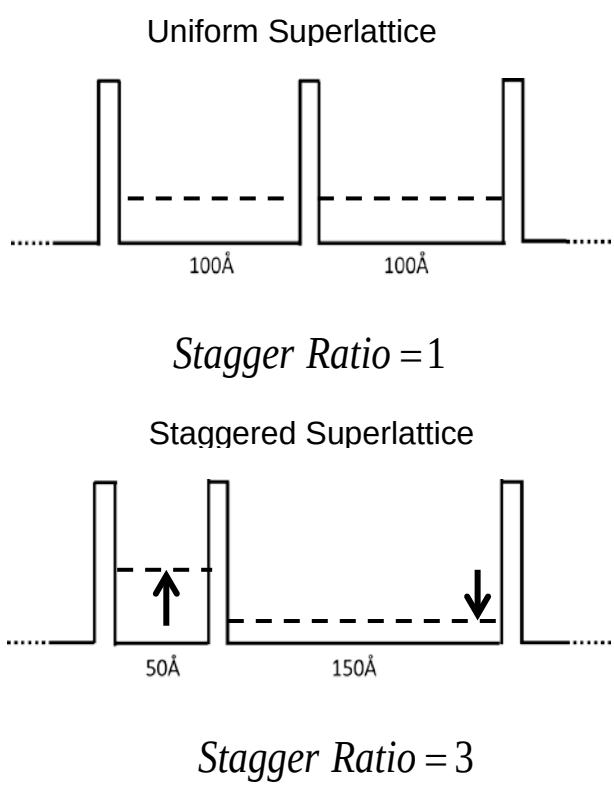

Figure III-7: Diagram of one period of a staggered and unstaggered superlattice. The staggering ratio is the wide well thickness divided by the thin well thickness

This model has been used to design alternate superlattice structures. As seen in figure III-6, the QSE decreases as the well width increases. However, as previously found, the barrier thickness is limited to about 30Å. This has been

overcome by staggering adjacent wells, as seen in figure III-7 [17]. This structure keeps the amount of InGaAs and GaAsP in the superlattice the same, which maintains the strain balance condition. However, since one well is made thicker at the expense of another, the QSE is reduced in the thicker well. The staggering ratio is a measure of the extent of this thickness shift. It should also be noted that the barrier thickness remains the same, so carrier transport is unaffected. Staggered devices have been grown and fabricated, showing a significant extension in the superlattice band edge, as will be shown in the next section. Additionally, the second electron state becomes visible when the band edge is extended, which adds the benefit of increased absorption in this state due to the step-like shape of the quantum well density of states. Figure III-8 shows the predicted band edge for several different staggering ratios.

III-3 Future Work

There are several directions that could be taken in future modeling. The magnitude of free carrier and excitonic absorption has already been calculated and has been found to roughly agree with the absorption seen in our devices. This, along with the IQE calculations could be used to calculate the EQE of devices. By comparing this to experimental EQEs would further validate our models and help to determine how particular superlattices enhance or degrade the performance of actual devices. It could also be used to simulate the effect of higher solar concentrations and the expected impact of the structure in a fully fabricated multijunction device. All of these techniques could also be adapted to analyze a similar InGaP-SLS top cell in order to improve the performance of that junction.

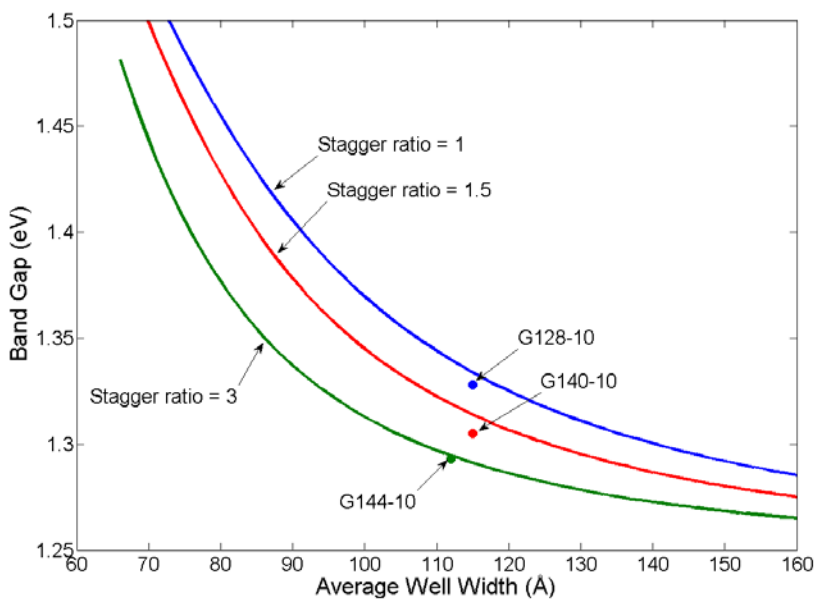

Figure III-8: Band edge energy for superlattices with several staggering ratios. Corresponding samples show good agreement with theory.

IV. Device Characterization

In this section we will discuss device fabrication and the different electrical characterization techniques used on our SLS devices, their importance, and significant findings related to each. The primary characterization methods used are light/dark current-voltage, spectral response, and capacitance-voltage measurements. We have also studied the effects of temperature and reverse bias on the SLS devices.

IV-1 Device Fabrication

Geometry

Upon completion of material growth and characterization, solar cell devices were fabricated in our modular clean room in order to characterize the electrical properties of the devices. This room houses the hot plates, photoresist spin coater and mask aligner which allows for the front contacts to be defined and developed. We use an electron beam gun evaporation unit and the metal contacts to be evaporated onto the devices. During this project we have used two different types of devices geometries and sizes. The first device geometry used was a basic, one bus-bar type of device as depicted in Figure IV-1. The device mesa size is 2.5 mm × 2.5 mm. While this device geometry is suitable for understanding whether the devices work well or not, it does have some drawbacks. These include a high series resistance due to the grid line pitch and line width (~12 µ) the fact that the lines do not cover the entire device, and lateral resistance. The wider grid lines shade more of the active area and reduce the short circuit current of the device as well. We have adopted a more modern grid used by several leaders in the concentrator photovoltaic industry, including Spire. This device geometry can be seen in Figure IV-2. In this design, the grid line width is 5µm with a grid pitch of 120µm. This design appropriately balances line with and pitch to reduce series resistance while maximizing the active area. The total mesa area used is 1.5 mm × 1.5 mm. This type of structure is better suited for high solar concentration.

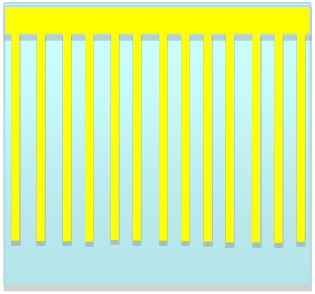

Figure IV-0-1: Previously used solar cell device geometry

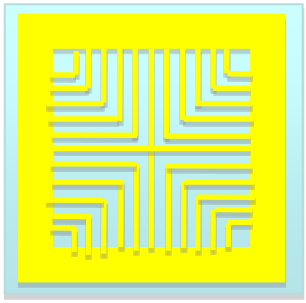

Figure IV-2: Current solar cell device geometry that exhibits good balance between series resistance and obscuration

Ohmic Contacts

We investigated the type of metal schemes to create ohmic contacts for the devices based on literature review and experimental measurements of specific contact resistance. The standard Ti/Pt/Au contact for p-type GaAs is very expensive for research purposes so we chose to use a similar scheme that uses Ti/Pd/Ag with thicknesses of 500 Å/1000 Å/3500 Å. The thickness of the silver was varied for different measurements to reduce the series resistance of the lines. For the n-type contacts we used the standard Ni/AuGe/Ni/(Ag) contact, except replacing the thicker cap layer with silver. The thicknesses of these layers were 50 Å/1000 Å/350 Å/3500 Å. Transmission Line Method (TLM) structure measurements revealed that the lowest specific contact resistance was obtained by annealing these contacts at 400°C

for 30 seconds. For our metal scheme and annealing procedure we were able to obtain specific contact resistances in the low 10^{-5} Ω-cm^2.

IV-2 Spectral Response

Spectral response measurements were performed to determine the external quantum efficiency (EQE) versus different wavelengths of the solar cells devices. EQE gives an indication of the potential for current gain based on how far the SLS extends absorption past that of a GaAs control sample and how high the EQE for the extension is. To maximize current gain, the EQE for the extension should be as far reaching and high as possible. This is accomplished by incorporating more periods within the SLS structure. Absorption within a multi-quantum well structure is determined by the number of quantum wells. Figure IV-3 shows a GaAs control sample and SLS device with $In_{0.15}Ga_{0.85}As$ wells and ~30 Å $GaAs_{0.2}P_{0.8}$ barriers having wavelength extension out to ~950 Å. Just as significant as the absorption extension though is the fact that incorporating the SLS device shows no change in EQE (within experimental error) from the GaAs control device. This indicates that carrier transport of carriers generated within the InGaAs wells and minority carriers generated within the base and emitter regions is near 100%. As indicated in the modeling section, the barriers in this device are thin enough to allow for efficient tunneling to take place. The amount of absorption in the i-layer is related to the number of wells incorporated in to the depletion region. Figure IV-4 shows that increasing number of wells increases the absorption amount beyond that of GaAs.

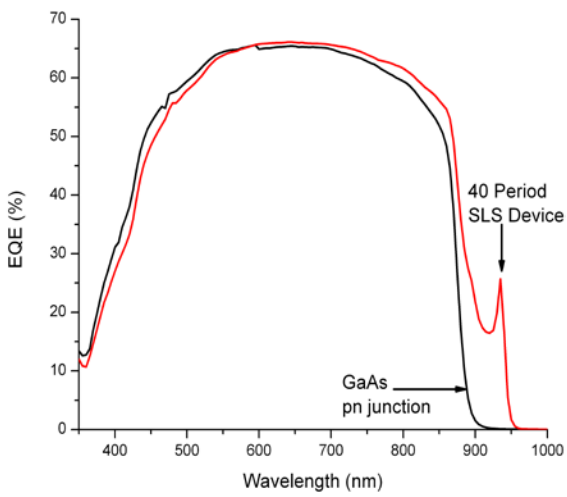

Figure IV-3: Spectral response of a uniform SLS device showing extension out to 950 nm.

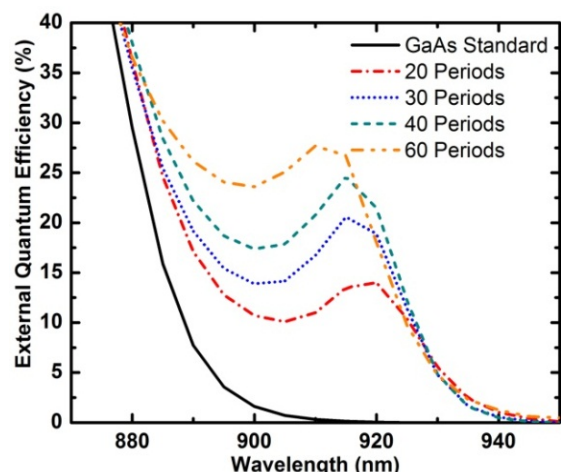

Figure IV-4: Spectral response of several SLS devices showing increased absorption with increased number of quantum wells incorporated into the SLS.

Staggering the well thicknesses, as was discussed in section III, reduces quantum size effects and extends absorption towards longer wavelengths than that which can be achieved with a uniform SLS. As the stagger ratio increases, longer wavelengths can be absorbed as seen in the Figure IV-5.

However, if we plot the wavelength extension versus stagger ratio, as seen in Figure IV-6 we see that there is a diminishing return when the stagger ratio increases beyond 3. This is important because it also becomes more difficult to grow the structures with higher stagger ratio. We have therefore concluded

that a stagger ratio of 3 is most appropriate to increase cutoff wavelength while maintaining high quality material.

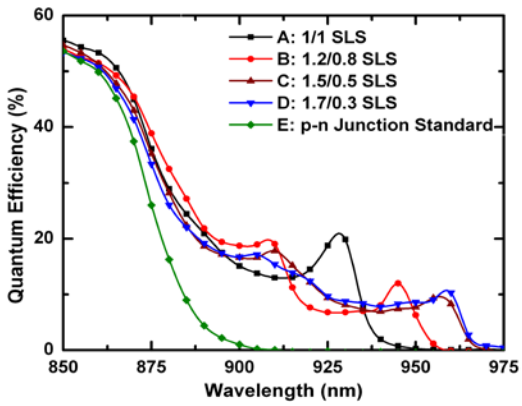

Figure IV-5: Spectral response of a GaAs control compared to SLS devices with differing stagger ratios.

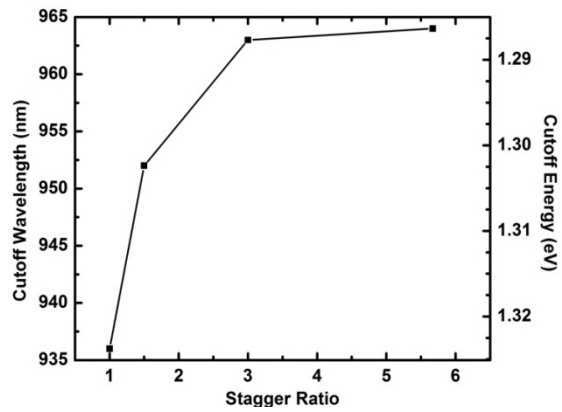

Figure IV-6: Cutoff wavelength/energy vs stagger ratio of staggered SLS devices

IV-3 Current-Voltage (J-V)

Illuminated Current-voltage (J-V) measurements were performed on the solar cell devices to obtain the short circuit current density (J_{SC}), open circuit voltage (V_{OC}), fill factor (FF), and series/shunt resistance.

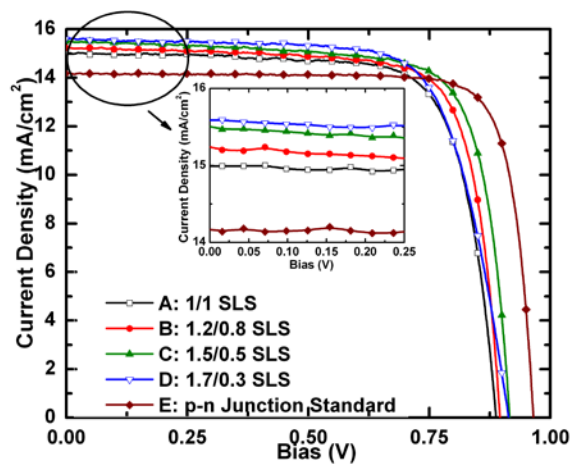

Figure IV-7: J-V characteristics for GaAs control and staggered SLS devices with varying stagger ratios

As stated, the goal of incorporating the SLS structure within a GaAs device is to increase the current density without significantly reducing open circuit voltage or fill factor. Figure IV-7 shows a comparison of a GaAs control sample, a device with a uniform SLS, and several devices with a staggered SLS. These devices correspond with the devices shown in the spectral response section above. All SLS devices have $In_{0.15}GaAs$ wells (thicknesses varied based on stagger ratio) with ~30 Å $GaAs_{0.2}P_{0.8}$ barriers. Inspection of this plot reveals that increasing the stagger ratio does in fact increase the J_{SC} without significantly affecting the V_{OC} or FF. However, as with the spectral response, there is a diminishing increase with increasing stagger ratio. These devices used the older grid geometry and therefore suffer from excess metallization and no anti-reflection coating. As a result, the current density is relatively low. We have grown and fabricated a 60 period device that showed tremendous current density gain as shown in Figure IV-8. An increase of ~3.5 mA/cm^2 is observed. This current gain is achieved with only about 30 mV drop in the open circuit voltage. Taking into account the lack of AR coating, we can expect an increase of 4.5 mA/cm^2 with AR coating, as seen in Figure IV-9. Efforts are still underway to improve fill factor. This may be the highest current gain reported in the GaAs middle cell due the addition of SLS

Although some devices exhibit good V_{OC} and fill factor, some devices such as the SLS device with 23% indium wells seen in Figure IV-10 have severe shunt resistance. This shunt resistance is likely caused by a slight relaxation due to the used of staggering and may have wells thicker than the critical layer thickness.

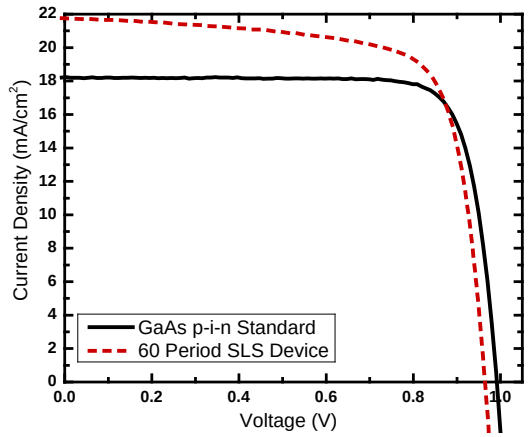

Figure IV-8: J-V characteristics of a 60 period SLS device showing significant gain in J_{SC}

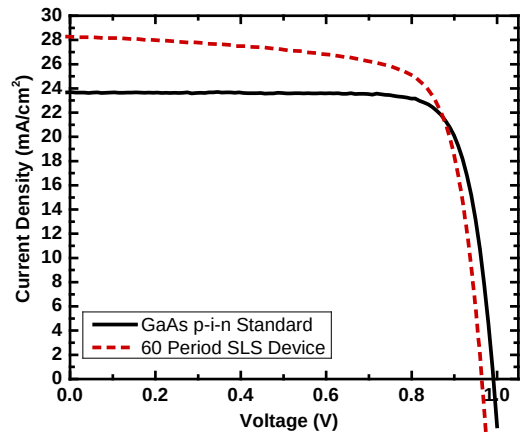

Figure IV-9: J-V characteristics of a 60 period SLS corrected for AR coating showing ~4.5 mA/cm^2 increase in short circuit current

Superlattice Devices under Concentration

We have performed light J-V measurements at higher solar concentrations up to ~70 suns, shown in Figure IV-11. In an effort to see the effects of the SLS we have normalized the curves for an SLS device under one sun and 70 suns; otherwise it is very difficult to see relative changes in the shape of the J-V curve due to large increase in J_{SC}. Although the one sun V_{OC} is not as high as we normally see on our devices, there is a significantly rise in V_{OC}, around 100 mV. This is, however, accompanied by a 5% decrease in the fill factor. Efforts are underway to investigate if the apparent series resistance is due to emitter sheet resistance, top side ohmic contacts, or from the SLS itself

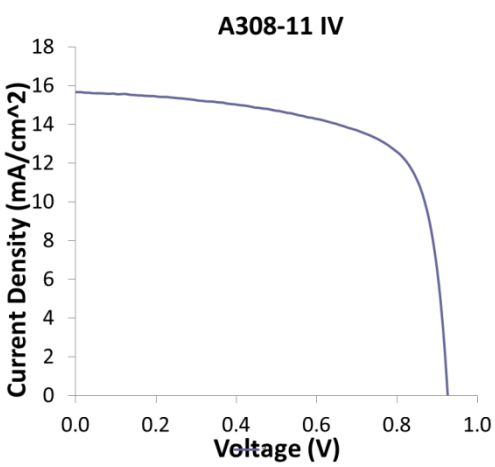

Figure IV-10: J-V characteristics of a 20 period staggered SLS device with 23% indium quantum wells

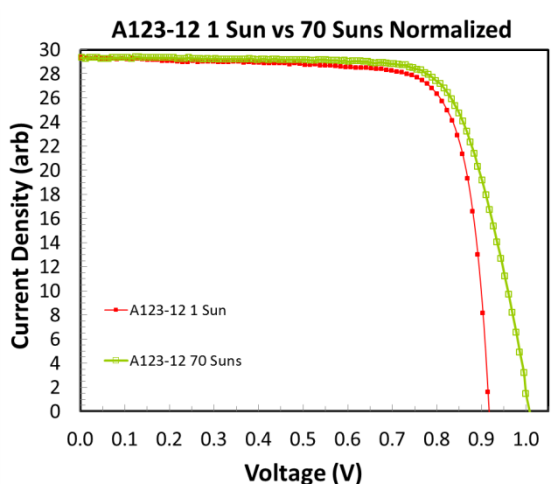

Figure IV-11: Normalized J-V curve for a SLS device under one sun and 70 sun illumination

IV-4 Effect of Barrier thickness

Spectral Response

One of the most important parameters of the SLS is the barrier thickness. It is necessary to grow a barrier thick enough so that the well width can be maximized but it is also critical that the barrier still be thin enough that carriers can readily tunnel through them. We have performed a study to show the effects of barrier thickness on the spectral response and J-V characteristics of SLS devices. Figure IV-12 shows the spectral response of a GaAs control sample, a 20 period thin barrier SLS device, and a thick barrier SLS device, as previously mentioned in section III. The spectral response shows a clear degradation in the EQE of the thick barrier device towards longer wavelengths whereas the thin barrier device is unaffected throughout the entire spectrum. These particular devices are n on p which means that hole minority carriers are generated within the emitter and electron minority carriers are generated within the base. This is significant because it reveals the limiting carrier of the device for the thick barrier device. For wavelengths shorter than about 600 nm, nearly 100% of the light will be absorbed within half a micron, which happens to be about the same thickness as the emitter. This means that wavelengths shorter than 600 nm will only generate hole minority carriers. Since the EQE at and below 600 nm is relatively unaffected compared to the GaAs control sample, we can therefore conclude that hole minority carriers generated within the emitter are transporting across the superlattice structure relatively unimpeded. On the contrary, only wavelengths of light longer than 600 nm are absorbed in the base. Increasing the light wavelength increases the penetration depth of the light. As the wavelength, and penetration depth, increases a larger portion of the total light is absorbed in the base where electron minority carriers are generated. Therefore longer wavelengths of light generate an increasing number of electron minority carriers. The spectral response of the thicker barrier reveals that the electron minority carriers generated in the base have a harder time transporting across the entire superlattice and are therefore the limiting minority carrier.

Device Polarity

To prove that electrons are in fact the limiting carrier in transport across the SLS, we grew a device with the opposite polarity, a p on n device, with barriers roughly the same thickness as in the previous section. In this device, the electron minority carriers are generated within the emitter. The primary difference here is that that <u>all</u> wavelengths contribute to minority carrier generation in the emitter.

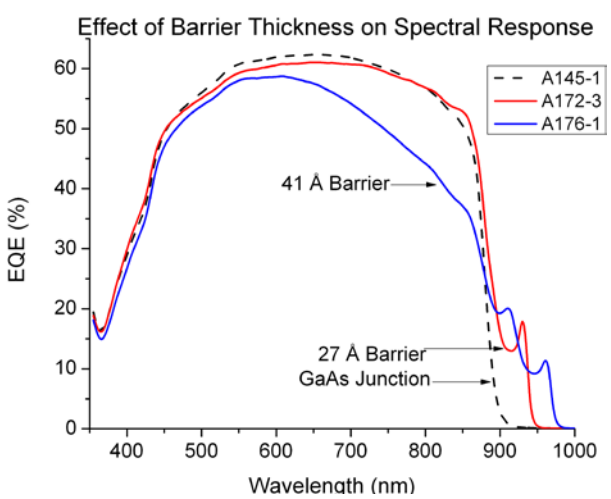

Figure IV-12: Spectral response curves of SLS devices with thin and thick barriers

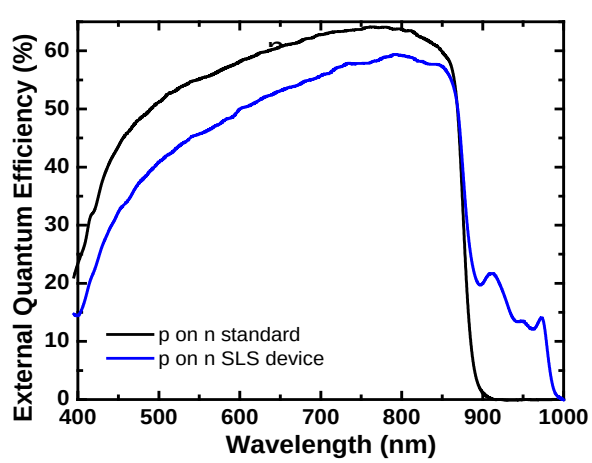

Figure IV-13: The effect of device polarity on the spectral response of SLS device. P on n devices exhibit a reduced response at all wavelengths below 870nm.

Since this is the case we would expect a reduced EQE at all wavelengths instead of only wavelengths that contribute to current in the base. Figure IV-13 shows the spectral response of this device and does indeed show this trend.

Dark and Light J-V

Dark J-V measurements were also used to examine the effect of barrier thickness. In principle, we should expect that a thicker barrier that reduces tunneling probability would lead to an increase in the recombination within the wells. An increase of recombination within the wells will lead to a higher dark current. According to the equation

$$V_{OC} = \frac{nk_B T}{q} \ln\left(\frac{J_{SC}}{J_0}\right)$$

a higher dark current will reduce the V_{OC} of the device. Figure IV-14 shows the dark current for a GaAs control sample, a thin barrier device, and a thick barrier device. This shows that by incorporating any SLS structure the dark current increases. However, the dark current in the region of n≈2.2 for the thicker barrier device is higher than that of the thin barrier device and is likely caused by an increase of recombination within the wells that occurs from a decrease in tunneling probability across the thicker barriers. We would expect this increase to further reduce the V_{OC}.

The light J-V characteristics also reveal important information as shown in Figure IV-15. The "thin" barrier device shows an increase in J_{SC} with minimal impact on V_{OC}. However, the "thick" barrier device shows what looks like severe shunt and series resistance. We believe that the shunt resistance could perhaps be due to the fact that the material quality in the thicker barrier, and hence thicker wells, may not be as good as the thinner barrier device. This may lead to some shunt resistance. While the device may look like it has severe series resistance we believe that this is likely due to a reduced electric field across the SLS as forward bias is increased. As forward bias is increased the probability of carrier transport is reduced further, which reduces the total current of the device.

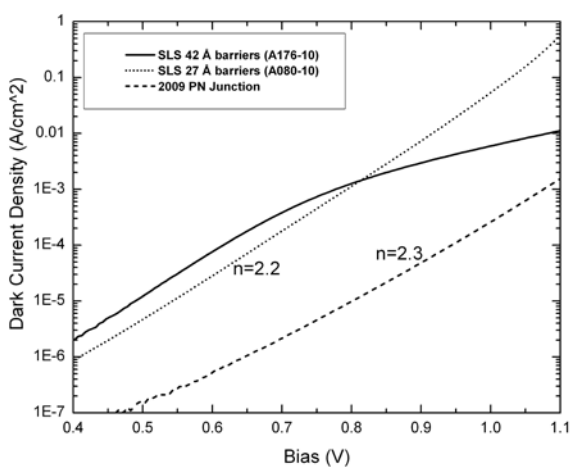

Figure IV-14: Dark current measurements for GaAs control as well as SLS devices with thin or thick barriers.

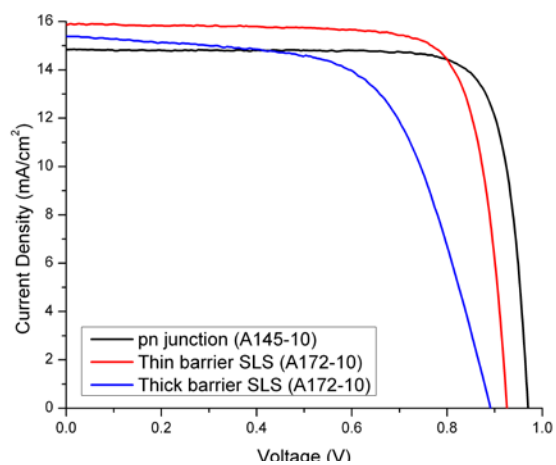

Figure IV-15: J-V characteristics showing the effects of barrier thickness.

IV-5 Capacitance-Voltage

C-V measurements allow us to determine the thickness of the depletion layer. The equation $C = \frac{\varepsilon A}{W}$, where C is the capacitance, ε is the relative permittivity time the permittivity in free space, A is the device area, and W is the width of the depletion region. This measurement becomes particularly important when growing thick superlattices with many periods. It is important that all of the SLS remain located within the built-in electric field of the device in order to facilitate carrier transport. Ideally, the depletion region would be completely void of charge in which case the depletion thickness would only be limited by the total strain buildup of the superlattice itself. However, unintentional background impurities are incorporated into "undoped" regions during growth. This places a limit on the maximum width and hence the width of the region with an electric field. By performing a C-V sweep, the width of the depletion region can be intentionally varied. Figure IV-16 shows an example of a C-V sweep (black

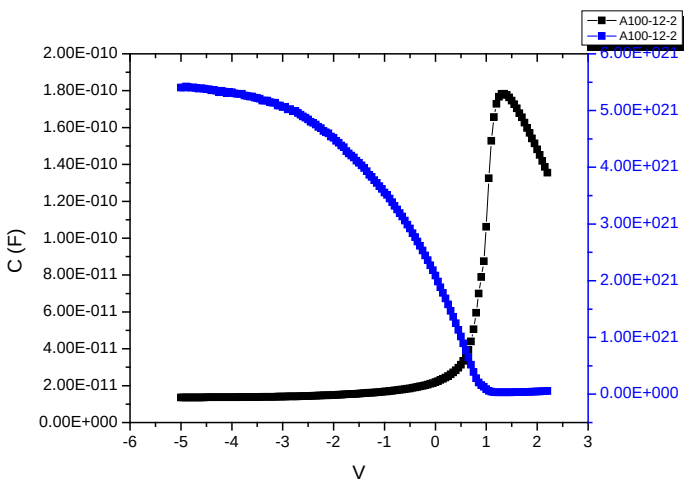

Figure IV-16: C-V (black) and $1/C^2$ (blue) curves for a 40 period SLS device with 23% indium.

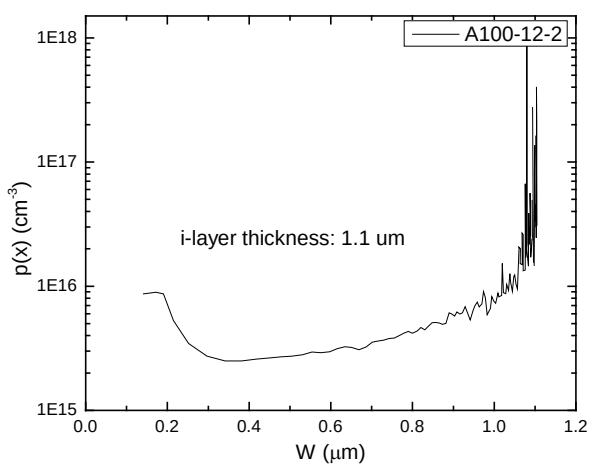

Figure IV-17: Doping density profile of a 40 period SLS device with 23% indium.

line) together with the $1/C^2$ curve (blue line). The derivative of the $1/C^2$ curve can be used to calculate the apparent doping density of the depletion region at a given location, which depends on the applied bias. Putting together the apparent doping density with the depletion width at a given bias reveals a doping profile, as seen in Figure IV-17.

We have, however, found an interesting trend that occurs when growing superlattices with increased indium composition within the wells. Figure IV-18 shows that as the indium content in the well increases, the maximum depletion with possible decreases significantly. In this experiment we intentionally grew thick superlattices to

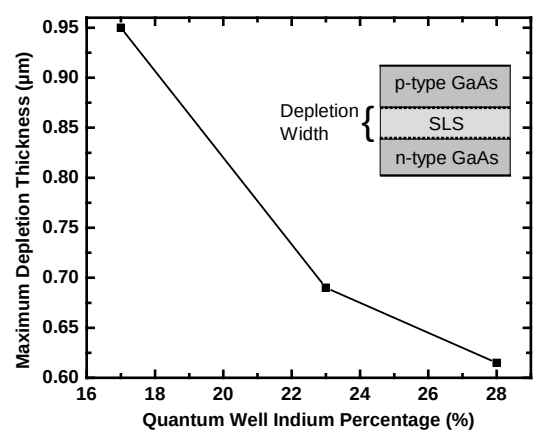

Figure IV-18: C-V meaurements were used to determine the maximum depletion region thickness as a function of indium composition within the wells.

find the maximum depletion thickness but did not expect to see such a drastic increase. The cause of this is still under investigation but could be due to an increase in defects in the material or relaxation within the structure.

IV-6 Electroluminescence

We have examined a unique method of characterizing the solar cells. We have performed electroluminescence (EL) measurements on devices and compared them with the spectral response of that same device. In order to perform this, the device is driven at high currents to inject enough carriers into the wells so that high enough recombination takes place within the wells to get light emission. The output is then measured by a spectrometer. This is useful in determining a relative tunneling probability between two different SLS structures. For instance, a SLS that has very good transport will exhibit a much lower EL peak amplitude than one with poor transport since the tunneling probability of the good SLS will be much higher and less recombination leading to light emission will occur. We can see here in Figure IV-19 that recombination in is much higher for SLS with high indium content, although this is not surprising because subsequent C-V results revealed that the 23% and 28% indium SLS devices were not fully depleted.

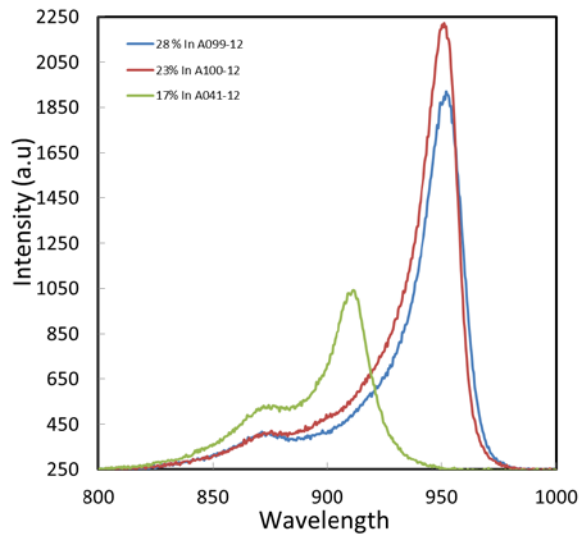

Figure IV-19: Electroluminescence of SLS devices with varying indium concentration

IV-7 Anti-Reflection Coating

We have applied a single layer anti-reflection (AR) coating to a device and see significant gains in the EQE, as seen in Figure IV-20. This particular AR uses Al_2O_3 which has a relatively low index of refraction. The predicted current gain, based on an integration of the EQE curve, is around 25%. The large drop off in EQE below 550 nm is due to slight absorption of the window at the direct band gap of the AlGaAs.

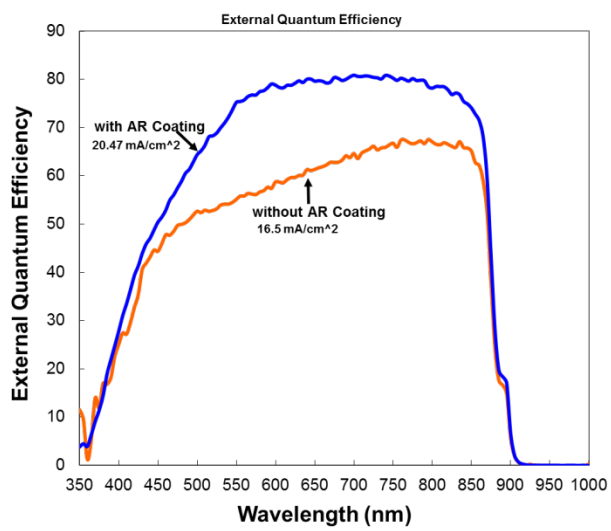

Figure IV-20: A SLS device with and without an anti-reflection coating. The AR coating used was a single layer of Al_2O_3.

IV-8 Future Work

1) *Double layer AR coating*

   Although the single layer AR coating improved the current gain of our device by about 25%, we can expect even higher gains by using a double layer AR (DLAR) coating. We are investigating DLAR coating schemes and can expect EQE gains of 30

to 35% depending on wavelength and overall current gain to be at least 30% higher. A potential DLAR scheme currently under investigation is the popular ZnS/MgF_2 scheme, but evaporating ZnS has proven to be relatively challenging given our current capabilities. We may look to alternatives to applying these coatings such as spin coating sol gels.

2) *Improve contact and series resistance*

   We will investigate other metal schemes and annealing temperature/time to improve contact resistance in order to lower the series resistance of the devices. Improving upon this will improve fill factor.

3) *Origin of shunt resistance*

   The origin of our shunt resistance is still under investigation. We do not necessarily visually see a correlation between surface morphology and shunt resistance. We may have to perform TEM to locate defects that may be causing this, although this can be difficult. We will perform a staircase C-V to see if there is a hysteresis of capacitance.

V. Bibliography

1. J. M. Olson, S. R. Kurtz, A. E. Kibbler, and P. Faine,"A 27.3% efficient $Ga_{0.5}In_{0.5}P$/GaAs tandem solar cell," Appl. Phys. Lett., vol. 56, no. 7, pp. 623-625, 1990.
2. R. R. King, D. C. Law, K. M. Edmondson, C. M. Fetzer, G. S. Kinsey, H. Yoon, R. A. Sherif, and N. H. Karam, "40% efficient metamorphic GaInP/GaInAs/Ge multijunction solar cells," Appl. Phys. Lett., vol. 90, p. 183516, 2007.
3. R. R. King, R. A. Sherif, D. C. Law, J. T. Yen, M. Haddad, C. M. Fetzer, K. M. Edmondson, G. S. Kinsey, H. Yoon, M. Joshi, S. Mesropian, H. L. Cotal, D. D. Krut, J. H. Ermer, and N. H. Karam, "New horizons in III-V multijunction terrestrial concentrator cell research," 21st. European Photovoltaic Solar Energy Conference, Dresden, Germany, 4-8 Sept. 2006.
4. S. R. Kurtz, A. A. Allerman, E. D. Jones, J. M. Gee, J. J. Banas, and B. E. Hammons, "InGasN solar cells with 1.0 eV band gap, lattice matched to GaAs," Appl. Phys. Lett., vol. 74, no. 5, pp. 729-731, 1999.
5. B. F. Moody, P. T. Barletta, N. A. El-Masry, J. C. Roberts, M. E. Aumer, S. F. LeBoeuf, and S. M. Bedair, "Effect of H_2 on nitrogen incorporation in the metalorganic chemical vapor deposition of $GaAs_{1-y}N_y$ ($0 \leq y \leq 0.08$)," Appl. Phys. Lett., vol. 80, no. 14, pp. 2475-2477, 2002.
6. M. Wanlas, P. Ahrenkiel, D. Albin, J. Carapella, A. Duda, K. Emery, D. Friedman, J. Geisz, K. Jones, A. Kibbler, J. Kiehl, S. Kurtz, W. McMahon, T. Moriarty, J. Olson, A. Ptak, M. Romero, and S. Ward, "Monolithic, ultra-thin GaInP/GaAs/GaInAs tandem solar cells," Photovoltaic Eneregy Conversion-IEEE 4th World Conference., vol. 1, pp. 729, 2006.
7. N. J. Ekins-Daukes, K. W. J. Barnham, J. P. Connolly, J. S. Roberts, J. C. Clark, G. Hill, and M. Mazzer, "Strain balanced GaAsP/InGaAs quantum well solar cells," Appl. Phys. Lett. vol. 75, no. 26, pp. 4195-4197, 1999.
8. T. Katsuyama, M. A. Tischler, D. Moore, N. Hamagichi, N. A. El-Masry, and S. M. Bedair, "New approaches for high efficiency cascade solar cells," *Solar Cells,* vol. 21, no. 1-2 pp. 413-418, 1987.
9. T. Katsuyama. S. M. Bedair, N. C. Giles, R. P. Burns, and J. F. Schetzina, "Growth and characterization of InGaAs/GaAsP strained layer superlattices," *J. Appl. Phys.,* vol. 62, vol 2, pp. 498-502, 1987.
10. J. W. Matthews and A. E. Blakeslee, "Defects in epitaxial multilayers," *J. Cryst. Growth*, vol. 27, pp. 118-125, 1974
11. B. F. Moody, "Strained Layer Superlattice Solar Cells," Ph.D. Dissertation, North Carolina State University, 2006.
12. Ekins-Daukes N.J., Kawaguchi K., Zhang J., "Strain-Balance Criteria for Multiple Quantum Well Structures and Its Signature in X-ray Rocking Curves", *Cryst. Growth Des.*, vol. 2, no. 4, pp. 287-292, 2002.
13. A. M. Fox, D. A. B. Miller, G. Livescu, J. E. Cunningham and W. Y. Jan, "Quantum well carrier sweep out: relation to electroabsorption and exciton saturation," *IEEE J. Quantum Electron.*, vol. 27, no. 10, pp. 2281-2295, 1991.
14. H. Schneider and K. v. Klitzing, "Thermionic emission and Gaussian transport of holes in a GaAs/$Al_xGa_{1-x}As$ multiple-quantum-well structure," *Phys. Rev. B*, vol. 38, no. 9, pp. 6160-6165, 1988.
15. G. K Bradshaw, C. Z. Carlin, J. P. Samberg, N. A. El-Masry, P. C. Colter, S. M. Bedair, "Carrier transport and improved collection in thin-barrier InGaAs/GaAsP strained quantum well solar cells," *IEEE J. Photovoltaics*, to be published.
16. P.-F. Yuh and K. L. Wang, "Formalism of the Kronig-Penny model for superlattices of a variable basis," *Phys. Rev. B*, vol.38, no. 18, pp. 13307-13315, 1988.
17. P. C. Colter, C. Z. Carlin, J. P. Samberg , G. K. Bradshaw and S. M. Bedair, "Staggered InGaAs/GaAsP strained layer superlattices for use in optical devices," *Phys. Status Solidi A*, vol. 208, no. 12, pp. 2884-2888, 2011.

VI. Publications List

Journal Articles

P. C. Colter, C. Z. Carlin, J. P. Samberg , G. K. Bradshaw and S. M. Bedair, "Staggered InGaAs/GaAsP strained layer superlattices for use in optical devices," *Phys. Status Solidi A*, vol. 208, no. 12, pp. 2884-2888, 2011.

G. K Bradshaw, C. Z. Carlin, J. P. Samberg, N. A. El-Masry, P. C. Colter, S. M. Bedair, "Carrier transport and improved collection in thin-barrier InGaAs/GaAsP strained quantum well solar cells," *IEEE J. Photovoltaics*, to be published.

Conference Proceedings

G. K. Bradshaw, C. Z. Carlin, P. C. Colter, J. L. Harmon, J. P. Samberg, and S. M. Bedair, "Effects of Barrier Width on Spectral Response of Strained Layer Superlattices for High Efficiency Solar Cells," *Mater. Res. Soc. Symp. Proc.*, vol. 1211, 2009.

J. P. Samberg, C. Z. Carlin, N. A. El-Masry, G. K. Bradshaw, P. C. Colter, J. L. Harmon, S. M. Bedair and J. R. Hauser, "Characterization of Strained Layer Superlattice Solar Cells by X-ray Diffraction and Current-Voltage Measurements," *Mater. Res. Soc. Symp. Proc.*, vol. 1211, 2009.

Presented Papers

C. Z. Carlin, J. P. Samberg, G. K. Bradshaw, N. A. El-Masry, P. C. Colter, S. M. Bedair. "The Optimization of High Indium and High Phosphorus Content InGaAs/GaAsP Strained Layer Superlattices for Use in Multijunction Solar Cells," *Conference Record, 38th IEEE Photovoltaic Specialists Conference,* Austin, June 2012; to be published.

Conference Presentations

C. Z. Carlin, G. K. Bradshaw, J. P Samberg, N. A. El-Masry, P. C. Colter, S. M. Bedair. "Investigation of the Transport Mechanism through InGaAs/GaAsP Strained Layer Superlattices." Presented at the 54th Electronic Materials Conference, University Park, PA, 2012.

J.P. Samberg, C.Z. Carlin, G.K. Bradshaw, P.C. Colter, N.A. El-Masry, S.M. Bedair. "Novel Superlattice Structures to Minimize Quantum Size Effects in Optoelectronic Devices." Presented at the 54th Electronic Materials Conference, University Park, PA, 2012.

Poster Presentations

G. K. Bradshaw, C. Z. Carlin, P. C. Colter, J. P. Samberg, N. El-Masry, S. M. Bedair. "Strained Layer Superlattices for Use in Multijunction Solar Cells." Presented at the North Carolina State University Graduate Symposium, Raleigh, NC, 2012.